Nuclear mass table in density functional approach inspired by neutron-star observations

Hana Gil,[1] Nobuo Hinohara,[2,3,4] Chang Ho Hyun,[5] and Kenichi Yoshida[6,2,7,*]

[1]*Center for Extreme Nuclear Matters, Korea University, Seoul 02841, South Korea*
[2]*Center for Computational Sciences, University of Tsukuba, Tsukuba, Ibaraki 305-8577, Japan*
[3]*Faculty of Pure and Applied Sciences, University of Tsukuba, Tsukuba, Ibaraki 305-8571, Japan*
[4]*Facility for Rare Isotope Beams, Michigan State University, East Lansing, Michigan 48824, USA*
[5]*Department of Physics Education, Daegu University, Gyeonsan 38453, South Korea*
[6]*Research Center for Nuclear Physics, Osaka University, Ibaraki, Osaka 567-0047, Japan*
[7]*RIKEN Nishina Center for Accelerator-Based Science, Wako, Saitama 351-0198, Japan*

(Received 31 March 2021; revised 16 July 2023; accepted 26 September 2023; published 20 October 2023)

Background: The nuclear energy-density functional (EDF) approach is widely employed to describe nuclear-matter equations of state (EoS) and the properties of finite nuclei. Recent advancements in neutron-star (NS) observations have imposed constraints on the nuclear EoS. The Korea-IBS-Daegu-SKKU (KIDS) functional has been then developed to satisfy the NS observations and applied to homogeneous nuclear matter and spherical nuclei.
Purpose: We examine the performance of the KIDS functional in this study by calculating the masses and charge radii of even-even nuclei towards the drip lines.
Method: The Kohn-Sham-Bogoliubov equation is solved by taking into account the axial deformation.
Results: The root-mean-square deviations of the binding energy and the charge radius for the KIDS models are 4.5–5.1 MeV and 0.03–0.04 fm, which are comparable to those for existing EDFs. The emergence and development of nuclear deformation in open-shell nuclei are well described. The location of the neutron drip line is according to the nuclear-matter parameter characterizing the low-mass NS.
Conclusions: The NS-observation-inspired EDF offers a reasonable reproduction of the structures of finite nuclei. A future global optimization that incorporates more nuclear data will enhance the accuracy and predictive power of neutron-rich nuclei.

DOI: 10.1103/PhysRevC.108.044316

I. INTRODUCTION

A microscopic construction of the nuclear equation of state (EoS) and its determination from nuclear experiments have been an interdisciplinary issue between nuclear physics and astrophysics [1–3]. Thanks to advances in astronomical observations, data on the properties of neutron stars (NS) have become more abundant, diverse, and precise [4–10]. There have been attempts to directly determine the EoS from observations using machine learning [11–14]. The bridging of recent data and nuclear structure properties is a new challenge in nuclear physics [15]. A desired model, which can describe both infinite nuclear matter and finite nuclei, must be able not only to reproduce the existing data accurately but also to be systematic at improving its predictive power and flexible to the addition of residual forces.

The self-consistent mean-field model rooted in nuclear density-functional theory is a promising framework as such a desired model [16]. A global calculation across the chart of nuclides has been carried out employing the existing energy-density functionals (EDFs) [17–20], and the optimization of a nuclear EDF has been performed [21–23]. Furthermore, the beyond-mean-field correlations have been considered [24,25].

As an intermediate step to bridge the low-energy nuclear structures and the astrophysical observations, the KIDS (Korea-IBS-Daegu-SKKU) density functional was applied to constrain the EoS by using state-of-the-art data on x-ray sources, low-mass x-ray binaries, and gravitational waves [26–28]. The symmetry energy thus determined is consistent with the results in the literature, and the ranges of the uncertainty could be reduced non-negligibly. In a subsequent work, an effect of the symmetry energy has been explored in finite nuclei by considering the Nd isotopes in the neutron-rich region [29]. We employed four models: KIDS-A, B, C, and D, each characterized by distinct levels of symmetry energy stiffness. The models agree well with the data on binding energy, charge radius, and quadrupole deformation. On the other hand, predictions in the neutron-rich regions such as the neutron skin thickness and the neutron drip line show a strong dependence on the symmetry energy. For a better understanding of the behavior of the model and the effect of the symmetry energy, extension of the analysis to the whole nuclear landscape is in due order.

In the present work, we investigate the properties of even-even nuclei for the atomic number Z from 8 to 110, and for the

*kyoshida@rcnp.osaka-u.ac.jp

TABLE I. Parameters of the nuclear matter EoS including the compression modulus K_0, and the symmetry energy parameters J, L, and K_τ are given in units of MeV.

	K_0	J	L	K_τ
KIDS-A	230	33	66	−420
KIDS-B	240	32	58	−420
KIDS-C	250	31	58	−360
KIDS-D	260	30	47	−360
SLy4	229.9	32.0	45.9	−322.8

neutron number N from the proton drip line to $N = 3Z$. Major concerns are 1) how well the KIDS model thus constructed by using the NS data works across the entire range of the nuclear chart, and 2) to explore the dependence on the symmetry energy and the ranges of its uncertainty of the KIDS model constrained by the modern NS data. We analyze the results for the binding energy, charge radius, quadrupole deformation, and neutron drip line. The mean accuracy of the model is similar to that of existing Skyrme models, but it is obviously inferior to the globally fitted mass models. The result opens a challenge to the KIDS density functional whether it can achieve an accuracy comparable to the globally fitted mass models.

The paper is organized in the following order. In Sec. II, we briefly introduce the models. Some details about the numerical calculations are also summarized. In Sec. III, we present the results and discuss them. We summarize the work in Sec. IV.

II. MODEL

In this work, we use four KIDS functionals, KIDS-A, KIDS-B, KIDS-C, and KIDS-D. There are nine parameters in the functional. In the first step, we start with the interaction energy density in the nuclear matter:

$$\begin{aligned}\mathcal{E}_{\rm mat}(\rho_0,\,\delta) &= \sum_{i=0}^{2}\alpha_i\rho_0^{2+i/3} + \delta^2\sum_{i=0}^{3}\beta_i\rho_0^{2+i/3}\\ &= \sum_{i=0}^{2}\alpha_i\rho_0^{2+i/3} + \rho_1^2\sum_{i=0}^{3}\beta_i\rho_0^{i/3},\end{aligned} \tag{1}$$

where ρ_0 is the nucleon isoscalar density, $\rho_n + \rho_p$, and δ is the neutron-proton asymmetry, $(\rho_n - \rho_p)/\rho_0 = \rho_1/\rho_0$. There are seven parameters: three α_i's are determined to produce the basic properties of the symmetric matter such as the saturation density $\rho_c = 0.16$ fm^{-3}, the binding energy per nucleon 16 MeV, and the incompressibility in the range 230–260 MeV. Four β_i's that are responsible for the EoS of asymmetric matter are determined to produce the radius of $1.4M_\odot$ neutron stars in the range 11.8–12.5 km within the empirical ranges of the symmetry energy parameters $J = 30$–34 MeV, $L = 40$–70 MeV, and $K_\tau = -480$––360 MeV. Table I summarizes the EoS parameters that are consistent with the assumed constraints for the nuclear matter. The values of the SLy4 functional [30] are included as a reference. Ranges of K_0, J, and L are wide enough to account for the effect of uncertainties from nuclear matter to the nuclear properties across the nuclear chart. The momentum-dependent and the spin-orbit functionals are given by

$$\mathcal{E}_{\rm mom} = \sum_{t=0,1} C_t^{\tau}\rho_t\tau_t + C_t^{\Delta\rho}\rho_t\Delta\rho_t + C_t^{J}\mathsf{J}_t^2, \tag{2}$$

$$\mathcal{E}_{\rm so} = \sum_{t=0,1} C_t^{\nabla J}\rho_t\boldsymbol{\nabla}\cdot\boldsymbol{J}_t, \tag{3}$$

where J_t and $\boldsymbol{J}_t$ are the spin-current and spin-orbit densities, and $t = 0$ and 1 correspond to the isoscalar and isovector terms. The coupling constants are determined from the relation with the momentum-dependent and spin-orbit interactions of the Skyrme-type force. We have one parameter for the momentum-dependent term (k parameter that determines both t_1 and t_2 [31]), and one parameter for the spin-orbit term (W_0). These two are fitted to six nuclear data (the energy per particle and the charge radius of ^{40}Ca, ^{48}Ca, and ^{208}Pb). Two more parameters are added in the pairing functional for neutrons and protons:

$$\mathcal{E}_{\rm pair} = \sum_{q=n,p}\frac{t_0'^{(q)}}{4}\left(1 - \frac{1}{2}\frac{\rho_0}{\rho_c}\right)|\tilde{\rho}^{(q)}|^2, \tag{4}$$

where $\tilde{\rho}^{(q)}$ is the neutron or proton pair density. The pairing parameters are adjusted to the three-point formula for the odd-even staggering centered at ^{156}Dy.

The total number of parameters in each model is 11, and their numerical values can be found in Ref. [29]. Then, the total energy functional is given as

$$\mathcal{E} = \mathcal{T} + \mathcal{E}_{\rm mat} + \mathcal{E}_{\rm mom} + \mathcal{E}_{\rm so} + \mathcal{E}_{\rm Coul} + \mathcal{E}_{\rm pair}, \tag{5}$$

where

$$\mathcal{T} = \frac{\hbar^2}{2m}\tau_0 \tag{6}$$

is the kinetic term, where τ_0 is the isoscalar kinetic density and $\hbar^2/2m = 20.7525$ MeV fm^2. We include the one-body center-of-mass correction with $m \to mA/(A-1)$. The Coulomb energy functional $\mathcal{E}_{\rm Coul}$ consists of the direct term and exchange term, and the Slater approximation is applied to the exchange term [32].

The KIDS models are implemented in the HFBTHO code [32] to solve the Kohn-Sham-Bogoliubov equation taking the axial deformation into account. The calculations are performed in the $N_{\rm max} = 20$ full spherical oscillator shells. To find the global-minimum solution, we start calculations from the initial configurations with the mass quadrupole deformation $\beta_2 = 0$ and ± 0.3. The quasiparticle (qp) states are truncated according to the equivalent single-particle energy cutoff at 60 MeV.

The KIDS functionals have been applied to the quasielastic scattering of an electron and a neutrino off a nucleus [33–35]. It is shown that the cross section is sensitive to and depends critically on the in-medium effective mass of the nucleon. The result demonstrates that the lepton-nucleus reactions can provide a unique channel to probe the nuclear dynamics and nuclear matter properties. The model gives the neutron skin thickness of ^{48}Ca and ^{208}Pb consistent with the

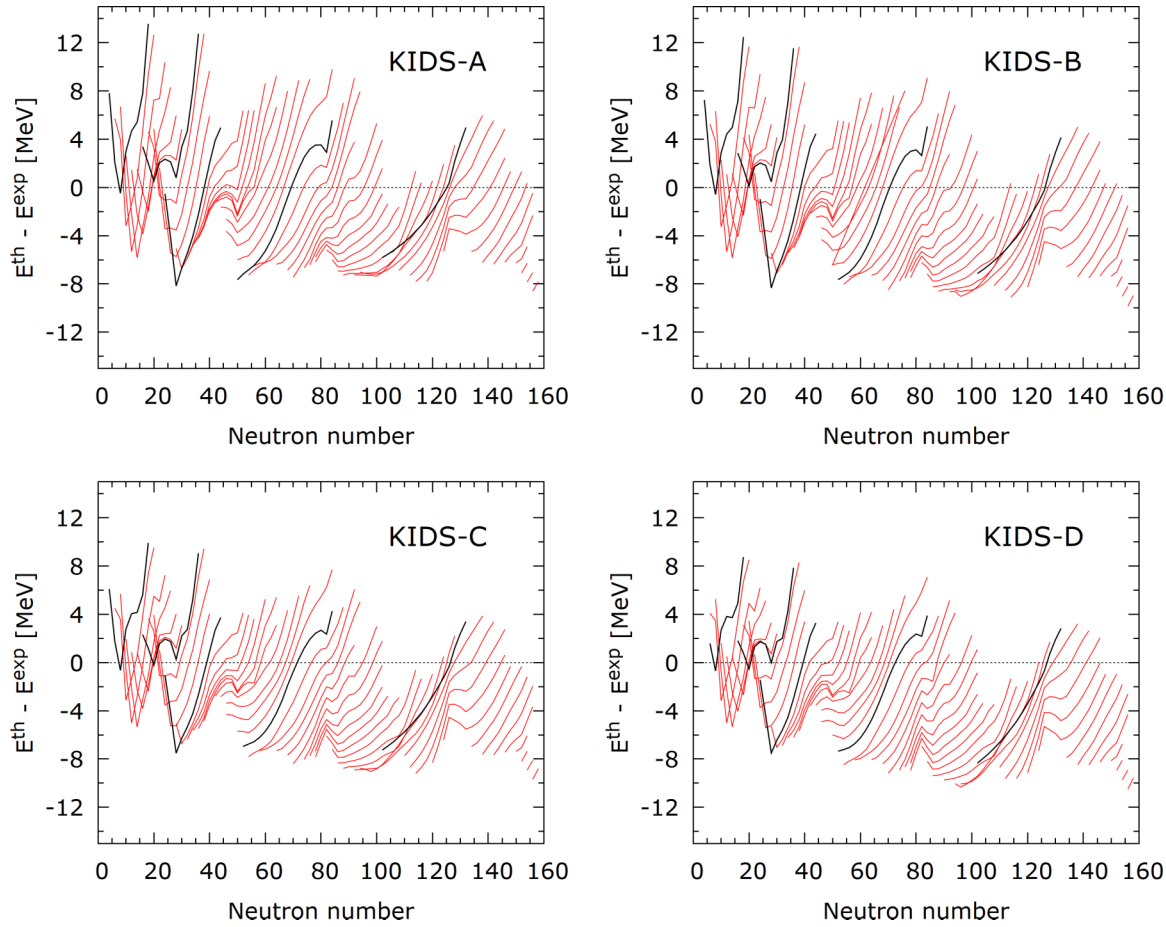

FIG. 1. Binding energy residuals between the KIDS results and experiment for 632, 630, 628, and 623 even-even nuclei for the KIDS-A, KIDS-B, KIDS-C, and KIDS-D models, respectively. The residuals are calculated only for the bound nuclei in each model among the available experimental data. Black lines denote the results for O, Ca, Ni, Sn, and Pb isotopes, respectively.

measurement from the dipole polarizability and interaction cross section [36].

III. RESULTS AND DISCUSSION

A. Binding energy

Figure 1 shows the calculated binding energies subtracted by the experimental data [37]. Here, the binding energy in Fig. 1 is given by

$$\mathrm{BE}(N,Z) = NM_n + ZM_p - M(N,Z), \tag{7}$$

where M_n and M_p are neutron and proton masses, and $M(N,Z)$ is the nuclear mass. The models KIDS-A–D show very similar patterns. Black lines denote the isotopic chains of O, Ca, Ni, Sn, and Pb. Since the models are fitted to the binding energy of ^{40}Ca, ^{48}Ca, and ^{208}Pb, two downward spikes in the line of Ca and $N = 126$ in the line of Pb are very close to zero. It is notable that decreasing and increasing behaviors are mixed in an isotopic chain for $N \lesssim 30$, but for $N \gtrsim 30$ each line shows a simply increasing behavior. In the light $N = Z$ nuclei between Ne and Ar, the calculation underestimates the binding energy, which results in the cusp. In heavier nuclei with $N > 30$, the cusp appears at the magic numbers. Slopes of the isotopic lines for a given nuclide look similar among the models KIDS-A–D. In Ref. [29], we investigated the origin of the increasing behavior of the residual as the neutron number increases in the isotopic chain of Nd. We found that by controlling the slope parameter L of the symmetry energy, it is possible to make the line of the Nd isotopes either flat or stiff. We thus expect that we can construct a mass model based on a KIDS-EDF with appropriate parameters.

We estimate the accuracy of the model in two ways. One is to evaluate the standard root-mean-square deviation (RMSD) defined by

$$\mathrm{RMSD}(O) = \sqrt{\langle (O_{\mathrm{th}} - O_{\mathrm{exp}})^2 \rangle}, \tag{8}$$

where O denotes an observable. Another measure is a difference between theory and experiment relative to the experimental data defined by

$$R(O) = 100 \times \frac{O_{\mathrm{th}} - O_{\mathrm{exp}}}{O_{\mathrm{exp}}}. \tag{9}$$

Table II summarizes the RMSD and R values of the KIDS model. The number of data included in the evaluation is 632, 630, 628, and 623 for the KIDS-A, KIDS-B, KIDS-C, and KIDS-D models, respectively. The number of data differs because the number of the bound-state solution is different

TABLE II. RMSD and R value of the KIDS models. RMSD(E) and RMSD(R_c) are in units of MeV and fm, respectively, and $\langle R(E)\rangle$ and $\langle R(R_c)\rangle$ are dimensionless.

Model	KIDS-A	KIDS-B	KIDS-C	KIDS-D
RMSD(E)	4.50	4.86	4.70	5.08
$\langle R(E)\rangle$	0.016	−0.068	−0.124	−0.208
RMSD(R_c)	0.0323	0.0356	0.0345	0.0384
$\langle R(R_c)\rangle$	−0.230	−0.414	−0.454	−0.599

depending on the model in the region close to the proton drip line. RMSD(E) values of the KIDS models are in the range 4.5–5.1 MeV. The accuracy is similar to that of the SLy4 model (4.8 MeV) [21], but larger than the DRHBc calculation with the PC-PK1 model (2.744 MeV) [38], and globally fitted mass models, e.g., 1.45 MeV of UNEDF0 [21]. We evaluate the average of R values over the results. Mean values of $R(E)$ in Table II indicate that the calculated binding energy deviates from the experimental data by 0.016%, −0.068%, −0.124%, and −0.208% on the average for the KIDS-A, KIDS-B, KIDS-C, and KIDS-D models, respectively. See the Supplemental Material, Ref. [39], for the numerical data.

B. Charge radius

Figure 2 shows the difference of charge radii $r_{\rm ch}^{\rm th} - r_{\rm ch}^{\rm exp}$. The charge radius is evaluated as

$$r_{\rm ch} = \sqrt{r_p^2 + 0.64\ {\rm fm}^2}, \tag{10}$$

where r_p^2 is the expectation value on the Hartree-Fock-Bogoliubov vacuum of a point proton radius, and the contribution from the finite proton size is included [32]. Table II summarizes the RMSD and R values for the charge radius. The number of data included in the evaluation is 344, 344, 343, and 343 for the KIDS-A, KIDS-B, KIDS-C, and KIDS-D models, respectively. The number of data depends on the model for the same reason as explained in the discussion of the binding energy. The experimental data are given in Refs. [40,41]. The deviation 0.032–0.038 fm is comparable to 0.032 fm obtained with the calculations with SLy4 [24] and PC-PK1 [38].

We find notable deviations in several regions. Except for light $N \approx Z$ nuclei, one sees an appreciable discrepancy in the $Z \approx 40$, 84, and 96 isotopes. The charge radius of the Sr, Zr, and Mo isotopes around $N = 60$ is calculated to be smaller than the measured one. This is because the calculations produce a spherical or weakly deformed configuration for the ground state, while a largely deformed configuration is suggested experimentally [42,43].

The calculated charge radius of the Po isotopes with $N = 108$ and 110 is also smaller than the measured value. The calculation produces a tiny oblate deformation with $|\beta_2| < 0.1$ whereas the SLy4 model predicts the oblate deformation with $|\beta_2| \approx 0.2$ [17].

On the other hand, the calculated charge radius of the Cm isotopes with $N = 146$–152 is larger than the measured one. The deviation is similar to the calculation with the DRHBc calculation with the PC-PK1 model [38].

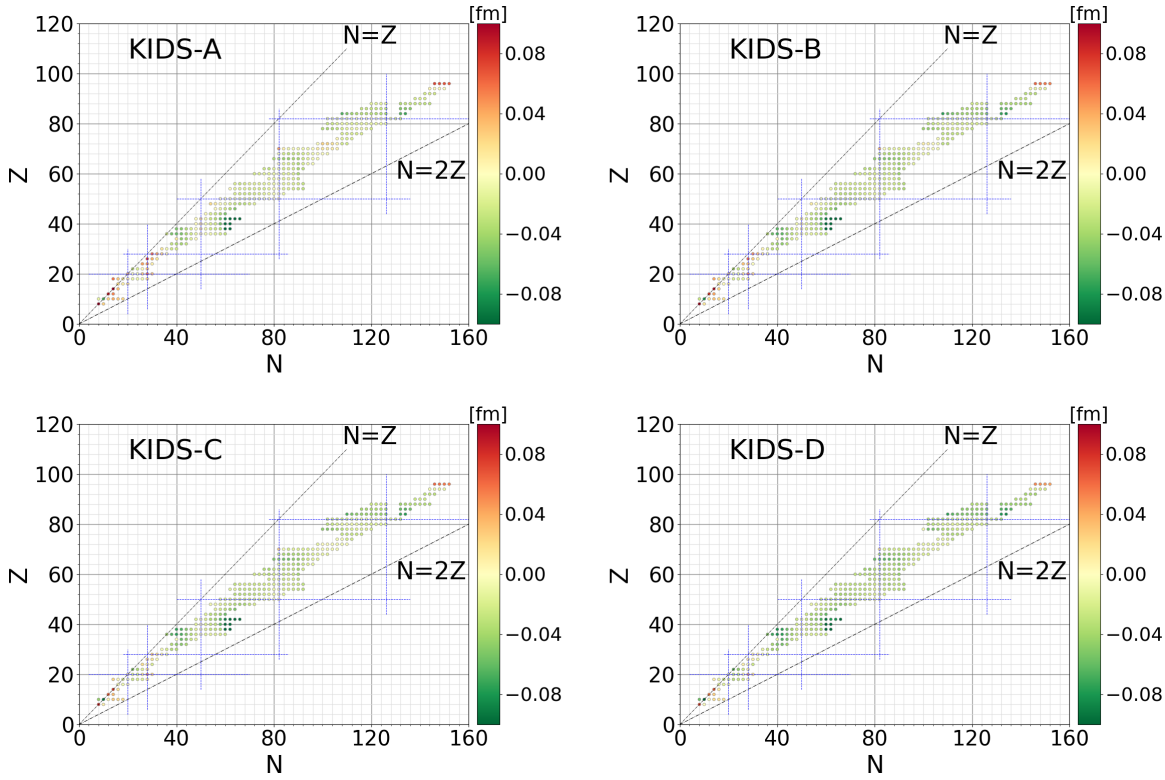

FIG. 2. Calculated charge radius difference from the experimental value for 344, 344, 343, and 343 even-even nuclei for the KIDS-A, KIDS-B, KIDS-C, and KIDS-D models, respectively.

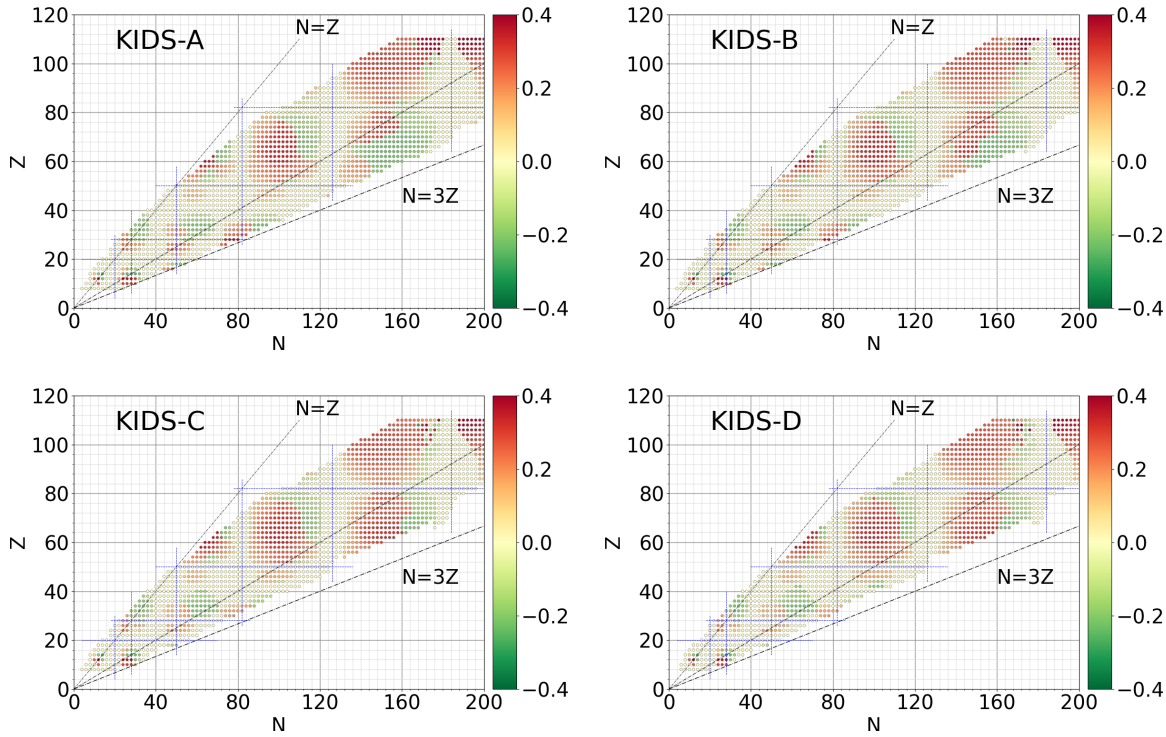

FIG. 3. Calculated quadrupole deformation $\beta_{2,p}$ for bound nuclei obtained by employing the KIDS-A–D models.

C. Deformation

Stepping away from the magic numbers, the deformation appears and then develops by increasing the neutron or proton number. Existing EDF calculations have described well the evolution of deformation [17,38,44]. The present KIDS functionals, where deformed nuclei are not included in determining the coupling constants, also describe the onset and the development of deformation including the sign of quadrupole deformation, as shown in Fig. 3. The deformation parameter here is defined as

$$\beta_{2,p} = \sqrt{\frac{\pi}{5}} \frac{Q_{2,p}}{r_p^2}, \tag{11}$$

where $Q_{2,p}$ is the quadrupole moment of protons. A gradual change of deformation is produced not only in the Nd isotopes, which we have already discussed in our previous study [29], but in other lanthanides.

The disappearance of the magic numbers and the appearance of new magic numbers in exotic nuclei have been discussed both experimentally and theoretically [45]. The KIDS models give a spherical configuration for the neutron-rich nuclei with $N = 20$ as other EDF models do [17,38,44] in contrast to the measurements. For $N = 28$, the KIDS models describe well the evolution of shape from the oblate to prolate deformations toward a neutron drip line as in Refs. [46,47]. In a neutron-deficient side, an oblate configuration appears at $N = 28$, and the KIDS-A and B models produce the oblate deformation in ^{56}Ni.

A possible deformation of the Sn isotopes in the very neutron-rich region around $N = 100$ is predicted by some calculations [17,38,44]. However, the present calculation using the KIDS models predicts the spherical shape for all the Sn isotopes.

KIDS-A–D models predict the breaking of the $N = 50$ and 82 spherical magic numbers near the drip line. The breaking of the magic numbers is also seen in DRHBc calculation with the PC-PK1 model [38], while the SLy4 gives the spherical configuration there [17]. An oblate configuration appears in the ground state at $N \approx 50$, and a prolate configuration shows up at $N \approx 82$. The magnitude of deformation is the largest, and the deformed region is wide in the KIDS-A model. As an example, we show the potential energy surface (PES) of a doubly magic nucleus ^{78}Ni in Fig. 4. The ground state is soft against the quadrupole deformation with the KIDS models compared with the SLy4 functional. The KIDS-A model gives the softest PES.

D. Drip line

According to Fig. 3, the rare-earth nuclei with $60 \leqslant Z \leqslant 70$ and $90 \leqslant N \leqslant 108$ are prolately deformed. Thus, the structure change is gradual, and one can expect to see a global isospin dependence. Then, we show in Fig. 5 two-neutron separation energies S_{2n}. The KIDS models overestimate the experimental values of S_{2n} and show a smooth decrease as the neutron number increases. Note that the drip line has been confirmed up to the Ne isotopes [50]. The present KIDS models overestimate the position of the drip line even in the light region. Therefore, the neutron drip line of the rare-earth isotopes predicted by the KIDS models would be located on a more neutron-rich side than where in nature. In our previous analysis of the Nd isotopes, we found that the isotopic dependence of S_{2n} is grouped into two: Group 1 and Group 2 [29]; the

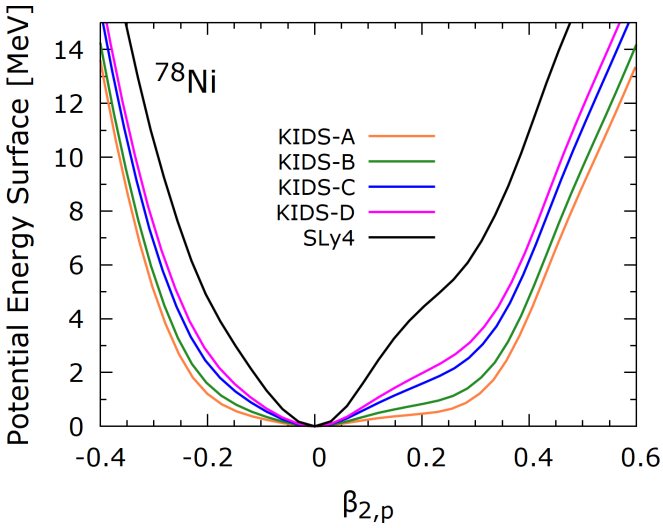

FIG. 4. Calculated PES of ^{78}Ni using the KIDS-A–D models. The result obtained by using the SLy4 functional is included.

KIDS-A–D models belong to Group 2. For $Z \approx 70$ isotopes, they show a similar isotopic dependence among Group 2. When decreasing the proton number, one can see that KIDS-C and D give a lower S_{2n} value than KIDS-A and B do in neutron-rich nuclei.

Figure 6 depicts the predictions for the neutron and proton drip lines. The drip line is determined by looking at the sign change in the chemical potential. In spite of the uncertainty of the symmetry energy, proton drip lines are similarly predicted by the models. When the drip positions differ between the models, the neutron numbers differ only by two at most. Therefore, models practically predict identical results for the proton drip line. The reason for the proton drip being insensitive to the symmetry energy is analyzed well with the

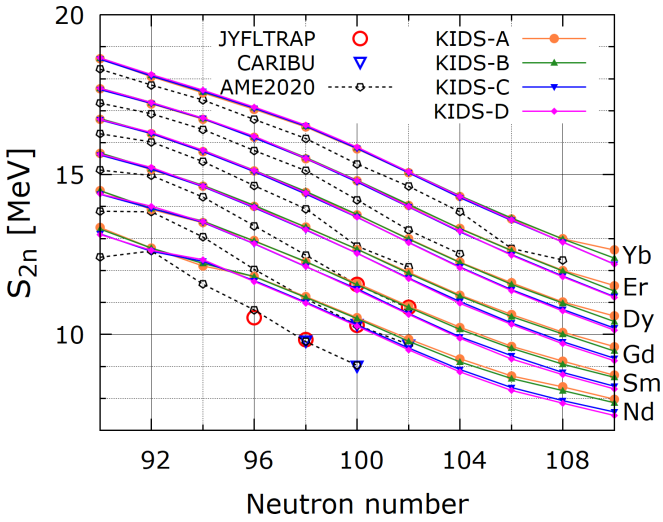

FIG. 5. Two-neutron separation energy S_{2n} of the rare earth isotopes with $Z = 60$–70. The experimental data for JYFLTRAP and CARIBU are obtained from Refs. [48,49], respectively.

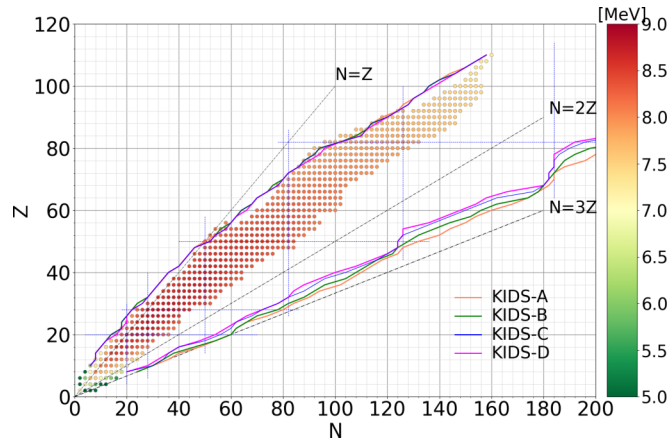

FIG. 6. Neutron and proton drip lines predicted by the KIDS models. Filled circles indicate the E/A value taken from AME2020 [37].

semiempirical mass formula in Ref. [51]. The KIDS models also agree well with the experimental data.

The drip line is located in a more neutron-rich region with the order KIDS-A $\gtrsim$ KIDS-B $>$ KIDS-C $\gtrsim$ KIDS-D. The order is the same as the magnitude of the parameter, which has been proposed for characterizing the structure of low-mass neutron stars: $\eta_\tau = (-K_\tau L^5)^{1/6}$ [52]. The η_τ value is 89.8, 80.7, 78.6, and 66.0 MeV for the KIDS-A, B, C, and D, respectively.

Looking into more details, one can see some features specific to each model. As a general trend, the difference in the position of the neutron drip line between models becomes large with the increase of the proton number. However, in a certain interval, the difference in the neutron between the models becomes four or less. Those small uncertainty regions are located at $Z = (8, 10, 12, 14)$, (22, 24), (44, 46, 48), and (68, 70, 72, 74), corresponding to $N \approx 28$, 64, 126, and 184. Small uncertainty regions are also obtained in the other EDFs. In Ref. [53], very small uncertainty happens at $N = 126$ and 184, and the reason is attributed to the spherical shell closure at these magic numbers. We obtain similar small uncertainties around $N = 28$ and 64, as well as $N = 126$ and 184.

IV. SUMMARY

The KIDS-A–D functionals were constructed based on the NS observations. It is noted that both nuclear matter properties and nuclear data are used in the decision of the model parameters, and the number of nuclear data used is much smaller than in the conventional models. The motivation for this different fitting scheme is to obtain a framework accurate and applicable to both infinite nuclear matter and finite nuclei. We have employed these functionals augmented by the mixed-type pairing-density functional to describe the properties of even-even nuclei across the nuclear chart. We have analyzed the results for the total binding energy, charge radius, quadrupole deformation, and the neutron drip line. The root-mean-square deviation for about 600 nuclei from the AME2020 data is as large as ≈5 MeV, which is compatible with widely used

nuclear EDFs but is larger than recently developed mass models. We have obtained a similar accuracy for the charge radii to the existing functionals. The appearance and development of nuclear deformation in open-shell nuclei are well described in spite of no deformed nuclei being considered in the construction of the KIDS functional. We have found that the location of the neutron drip line is according to the nuclear-matter parameter, $\eta_\tau = (-K_\tau L^5)^{1/6}$, characterizing the low-mass NS. The similarity of RMSD values to the widely used models indicates that a unified description of nuclear matter and finite nuclei is accessible in the KIDS framework. The results open a challenge to the KIDS functional whether it can achieve an accuracy comparable to the existing globally fitted EDF models.

ACKNOWLEDGMENTS

This work was supported by the NRF research Grants (No. 2018R1A5A1025563 and 2023R1A2C1003177), JSPS KAKENHI (Grants No. JP19K03824, JP19K03872, JP19KK0343, and JP20K03964), and the JSPS/NRF/NSFC A3 Foresight Program "Nuclear Physics in the 21st Century."

[1] X. Roca-Maza and N. Paar, Nuclear equation of state from ground and collective excited state properties of nuclei, Prog. Part. Nucl. Phys. **101**, 96 (2018).
[2] J. M. Lattimer and Y. Lim, Constraining the symmetry parameters of the nuclear interaction, Astrophys. J. **771**, 51 (2013).
[3] M. Oertel, M. Hempel, T. Klähn, and S. Typel, Equations of state for supernovae and compact stars, Rev. Mod. Phys. **89**, 015007 (2017).
[4] P. B. Demorest, T. Pennucci, S. M. Ransom, M. S. E. Roberts, and J. W. T. Hessels, A two-solar-mass neutron star measured using Shapiro delay, Nature (London) **467**, 1081 (2010).
[5] A. W. Steiner, J. M. Lattimer, and E. F. Brown, The equation of state from observed masses and radii of neutron stars, Astrophys. J. **722**, 33 (2010).
[6] A. W. Steiner, J. M. Lattimer, and E. F. Brown, The neutron star mass-radius relation and the equation of state of dense matter, Astrophys. J. Lett. **765**, L5 (2013).
[7] J. Antoniadis, P. C. C. Freire, N. Wex, T. M. Tauris, R. S. Lynch, M. H. van Kerkwijk, M. Kramer, C. Bassa, V. S. Dhillon, T. Driebe, J. W. T. Hessels, V. M. Kaspi, V. I. Kondratiev, N. Langer, T. R. Marsh, M. A. McLaughlin, T. T. Pennucci, S. M. Ransom, I. H. Stairs, J. van Leeuwen *et al.*, A massive pulsar in a compact relativistic binary, Science **340**, 1233232 (2013).
[8] H. T. Cromartie, E. Fonseca, S. M. Ransom, P. B. Demorest, Z. Arzoumanian, H. Blumer, P. R. Brook, M. E. DeCesar, T. Dolch, J. A. Ellis, R. D. Ferdman, E. C. Ferrara, N. Garver-Daniels, P. A. Gentile, M. L. Jones, M. T. Lam, D. R. Lorimer, R. S. Lynch, M. A. McLaughlin, C. Ng *et al.*, Relativistic Shapiro delay measurements of an extremely massive millisecond pulsar, Nat. Astron. **4**, 72 (2019).
[9] T. E. Riley, A. L. Watts, S. Bogdanov, P. S. Ray, R. M. Ludlam, S. Guillot, Z. Arzoumanian, C. L. Baker, A. V. Bilous, D. Chakrabarty, K. C. Gendreau, A. K. Harding, W. C. G. Ho, J. M. Lattimer, S. M. Morsink, and T. E. Strohmayer, A NICER view of PSR J0030+0451: Millisecond pulsar parameter estimation, Astrophys. J. Lett. **887**, L21 (2019).
[10] M. C. Miller, F. K. Lamb, A. J. Dittmann, S. Bogdanov, Z. Arzoumanian, K. C. Gendreau, S. Guillot, A. K. Harding, W. C. G. Ho, J. M. Lattimer, R. M. Ludlam, S. Mahmoodifar, S. M. Morsink, P. S. Ray, T. E. Strohmayer, K. S. Wood, T. Enoto, R. Foster, T. Okajima, G. Prigozhin *et al.*, PSR J0030+0451 mass and radius from NICER data and implications for the properties of neutron star matter, Astrophys. J. Lett. **887**, L24 (2019).
[11] D. Farrell, P. Baldi, J. Ott, A. Ghosh, A. W. Steiner, A. Kavitkar, L. Lindblom, D. Whiteson, and F. Weber, Deducing neutron star equation of state parameters directly from telescope spectra with uncertainty-aware machine learning, J. Cosmol. Astropart. Phys. **2023**, 016 (2020).
[12] Y. Fujimoto, K. Fukushima, and K. Murase, Mapping neutron star data to the equation of state using the deep neural network, Phys. Rev. D **101**, 054016 (2020).
[13] Y. Fujimoto, K. Fukushima, and K. Murase, Extensive studies of the neutron star equation of state from the deep learning inference with the observational data augmentation, J. High Energy Phys. 03 (2021) 273.
[14] F. Morawski and M. Bejger, Neural network reconstruction of the dense matter equation of state derived from the parameters of neutron stars, Astron. Astrophys. **642**, A78 (2020).
[15] J. Erler, C. J. Horowitz, W. Nazarewicz, M. Rafalski, and P.-G. Reinhard, Energy density functional for nuclei and neutron stars, Phys. Rev. C **87**, 044320 (2013).
[16] M. Bender, P.-H. Heenen, and P.-G. Reinhard, Self-consistent mean-field models for nuclear structure, Rev. Mod. Phys. **75**, 121 (2003).
[17] M. V. Stoitsov, J. Dobaczewski, W. Nazarewicz, S. Pittel, and D. J. Dean, Systematic study of deformed nuclei at the drip lines and beyond, Phys. Rev. C **68**, 054312 (2003).
[18] S. Hilaire and M. Girod, Large-scale mean-field calculations from proton to neutron drip lines using the D1S Gogny force, Eur. Phys. J. A **33**, 237 (2007).
[19] S. Goriely, S. Hilaire, M. Girod, and S. Péru, First Gogny-Hartree-Fock-Bogoliubov nuclear mass model, Phys. Rev. Lett. **102**, 242501 (2009).
[20] S. Goriely, S. Hilaire, M. Girod, and S. Péru, The Gogny-Hartree-Fock-Bogoliubov nuclear-mass model, Eur. Phys. J. A **52**, 202 (2016).
[21] M. Kortelainen, T. Lesinski, J. Moré, W. Nazarewicz, J. Sarich, N. Schunck, M. V. Stoitsov, and S. Wild, Nuclear energy density optimization, Phys. Rev. C **82**, 024313 (2010).
[22] M. Kortelainen, J. McDonnell, W. Nazarewicz, P. G. Reinhard, J. Sarich, N. Schunck, M. V. Stoitsov, and S. M. Wild, Nuclear energy density optimization: Large deformations, Phys. Rev. C **85**, 024304 (2012).
[23] G. Scamps, S. Goriely, E. Olsen, M. Bender, and W. Ryssens, Skyrme-Hartree-Fock-Bogoliubov mass models on a 3D mesh: Effect of triaxial shape, Eur. Phys. J. A **57**, 333 (2021).
[24] M. Bender, G. F. Bertsch, and P. H. Heenen, Global study of quadrupole correlation effects, Phys. Rev. C **73**, 034322 (2006).
[25] T. R. Rodríguez, A. Arzhanov, and G. Martínez-Pinedo, Toward global beyond-mean-field calculations of nuclear masses and low-energy spectra, Phys. Rev. C **91**, 044315 (2015).

[26] H. Gil, Y.-M. Kim, P. Papakonstantinou, and C. H. Hyun, Constraining the density dependence of the symmetry energy with nuclear data and astronomical observations in the Korea-IBS-Daegu-SKKU framework, Phys. Rev. C **103**, 034330 (2021).

[27] H. Gil and C. H. Hyun, Compression modulus and symmetry energy of nuclear matter with kids density functional, New Phys. Sae Mulli **71**, 242 (2021).

[28] H. Gil, P. Papakonstantinou, and C. H. Hyun, Constraints on the curvature of nuclear symmetry energy from recent astronomical data within the KIDS framework, Int. J. Mod. Phys. E **31**, 2250013 (2022).

[29] H. Gil, N. Hinohara, C. H. Hyun, and K. Yoshida, KIDS density functional for deformed nuclei: Examples of the even–even Nd isotopes, J. Korean Phys. Soc. **81**, 113 (2022).

[30] E. Chabanat, P. Bonche, P. Haensel, J. Meyer, and R. Schaeffer, A Skyrme parametrization from subnuclear to neutron star densities. Part II. Nuclei far from stabilities, Nucl. Phys. A **635**, 231 (1998); Erratum **643**, 441 (1998).

[31] H. Gil, Y. Oh, C. H. Hyun, and P. Papakonstantinou, Skyrme-type nuclear force for the KIDS energy density functional, New Phys.: Sae Mulli **67**, 456 (2017).

[32] M. V. Stoitsov, N. Schunck, M. Kortelainen, N. Michel, H. Nam, E. Olsen, J. Sarich, and S. Wild, Axially deformed solution of the Skyrme-Hartree-Fock-Bogoliubov equations using the transformed harmonic oscillator basis (II) HFBTHO v2.00d: A new version of the program, Comput. Phys. Commun. **184**, 1592 (2013).

[33] H. Gil, C. H. Hyun, and K. Kim, Quasielastic electron scattering with the KIDS nuclear energy density functional, Phys. Rev. C **104**, 044613 (2021).

[34] H. Gil, C. H. Hyun, and K. Kim, Inclusive electron scattering in the quasielastic region with the Korea-IBS-Daegu-SKKU density functional, Phys. Rev. C **105**, 024607 (2022).

[35] K. Kim, H. Gil, and C. H. Hyun, Quasielastic charged-current neutrino-nucleus scattering with nonrelativistic nuclear energy density functionals, Phys. Lett. B **833**, 137273 (2022).

[36] C. H. Hyun, Neutron skin thickness of ^{48}Ca, ^{132}Sn, and ^{208}Pb with KIDS density functional, New Phys. Sae Mulli **72**, 371 (2022).

[37] M. Wang, W. J. Huang, F. G. Kondev, G. Audi, and S. Naimi, The AME 2020 atomic mass evaluation (II). Tables, graphs and references, Chin. Phys. C **45**, 030003 (2021).

[38] K. Zhang *et al.* (DRHBc Mass Table Collaboration), Nuclear mass table in deformed relativistic Hartree–Bogoliubov theory in continuum, I: Even–even nuclei, At. Data Nucl. Data Tables **144**, 101488 (2022).

[39] See Supplemental Material at http://link.aps.org/supplemental/10.1103/PhysRevC.108.044316 for the numerical data of the binding energy, chemical potential, root-mean-square radius, quadrupole moment, and deformation parameter obtained by using the KIDS model.

[40] I. Angeli and K. Marinova, Table of experimental nuclear ground state charge radii: An update, At. Data Nucl. Data Tables **99**, 69 (2013).

[41] T. Li, Y. Luo, and N. Wang, Compilation of recent nuclear ground state charge radius measurements and tests for models, At. Data Nucl. Data Tables **140**, 101440 (2021).

[42] T. Sumikama, K. Yoshinaga, H. Watanabe, S. Nishimura, Y. Miyashita, K. Yamaguchi, K. Sugimoto, J. Chiba, Z. Li, H. Baba, J. S. Berryman, N. Blasi, A. Bracco, F. Camera, P. Doornenbal, S. Go, T. Hashimoto, S. Hayakawa, C. Hinke, E. Ideguchi *et al.*, Structural evolution in the neutron-rich nuclei ^{106}Zr and ^{108}Zr, Phys. Rev. Lett. **106**, 202501 (2011).

[43] J. Ha, T. Sumikama, F. Browne, N. Hinohara, A. M. Bruce, S. Choi, I. Nishizuka, S. Nishimura, P. Doornenbal, G. Lorusso, P.-A. Söderström, H. Watanabe, R. Daido, Z. Patel, S. Rice, L. Sinclair, J. Wu, Z. Y. Xu, A. Yagi, H. Baba *et al.*, Shape evolution of neutron-rich ^{106,108,110}Mo isotopes in the triaxial degree of freedom, Phys. Rev. C **101**, 044311 (2020).

[44] J. P. Delaroche, M. Girod, J. Libert, H. Goutte, S. Hilaire, S. Péru, N. Pillet, and G. F. Bertsch, Structure of even-even nuclei using a mapped collective Hamiltonian and the D1S Gogny interaction, Phys. Rev. C **81**, 014303 (2010).

[45] T. Otsuka, A. Gade, O. Sorlin, T. Suzuki, and Y. Utsuno, Evolution of shell structure in exotic nuclei, Rev. Mod. Phys. **92**, 015002 (2020).

[46] Y. Utsuno, T. Otsuka, B. A. Brown, M. Honma, T. Mizusaki, and N. Shimizu, Shape transitions in exotic Si and S isotopes and tensor-force-driven Jahn-Teller effect, Phys. Rev. C **86**, 051301(R) (2012).

[47] Y. Suzuki, W. Horiuchi, and M. Kimura, Erosion of $N = 28$ shell closure: Shape coexistence and monopole transition, Prog. Theor. Exp. Phys. **2022**, 063D02 (2022).

[48] M. Vilen, J. M. Kelly, A. Kankainen, M. Brodeur, A. Aprahamian, L. Canete, T. Eronen, A. Jokinen, T. Kuta, I. D. Moore, M. R. Mumpower, D. A. Nesterenko, H. Penttilä, I. Pohjalainen, W. S. Porter, S. Rinta-Antila, R. Surman, A. Voss, and J. Äystö, Precision mass measurements on neutron-rich rare-earth isotopes at JYFLTRAP : Reduced neutron pairing and implications for *r*-process calculations, Phys. Rev. Lett. **120**, 262701 (2018).

[49] R. Orford, N. Vassh, J. A. Clark, G. C. McLaughlin, M. R. Mumpower, G. Savard, R. Surman, A. Aprahamian, F. Buchinger, M. T. Burkey, D. A. Gorelov, T. Y. Hirsh, J. W. Klimes, G. E. Morgan, A. Nystrom, and K. S. Sharma, Precision mass measurements of neutron-rich neodymium and samarium isotopes and their role in understanding rare-earth peak formation, Phys. Rev. Lett. **120**, 262702 (2018).

[50] D. S. Ahn, N. Fukuda, H. Geissel, N. Inabe, N. Iwasa, T. Kubo, K. Kusaka, D. J. Morrissey, D. Murai, T. Nakamura, M. Ohtake, H. Otsu, H. Sato, B. M. Sherrill, Y. Shimizu, H. Suzuki, H. Takeda, O. B. Tarasov, H. Ueno, Y. Yanagisawa *et al.*, Location of the neutron dripline at fluorine and neon, Phys. Rev. Lett. **123**, 212501 (2019).

[51] R. Wang and L.-W. Chen, Positioning the neutron drip line and the r-process paths in the nuclear landscape, Phys. Rev. C **92**, 031303(R) (2015).

[52] H. Sotani and S. Ota, Neutron star mass formula with nuclear saturation parameters for asymmetric nuclear matter, Phys. Rev. D **106**, 103005 (2022).

[53] A. V. Afanasjev, S. E. Abgemava, D. Ray, and P. Ring, Nuclear landscape in covariant density functional theory, Phys. Lett. B **726**, 680 (2013).